Barium Oxide Encapsulating Cobalt Nanoparticles Supported on Magnesium Oxide: Active Non-noble Metal Catalyst for Ammonia Synthesis under Mild Reaction Condition

Katsutoshi Sato,*[a,b] Shin-ichiro Miyahara,[b] Kotoko Tsujimaru, [c] Yuichiro Wada,[c] Takaaki Toriyama,[d] Tomokazu Yamamoto,[d,e] Syo Matsumura,[d,e] Koji Inazu,[f] Hirono Mohri[g], Takeshi Iwasa,[a,h,i,j] Tetsuya Taketsugu,[a,h,i] and Katsutoshi Nagaoka*[a,b]

---

[a] Elements Strategy Initiative for Catalysts and Batteries, Kyoto University
1-30 Goryo-Ohara, Nishikyo-ku, Kyoto 615-8245, Japan
[b] Department of Chemical Systems Engineering, Graduate school of Engineering, Nagoya University
Furo-cho, Chikusa-ku, Nagoya 464-8603, Japan
[c] Department of Integrated Science and Technology, Faculty of Science and Technology, Oita University,
700 Dannoharu, Oita 870–1192, Japan
[d] The Ultramicroscopy Research Center, Kyushu University
Motooka 744, Nishi-ku, Fukuoka 819- 0395 (Japan)
[e] Department of Applied Quantum Physics and Nuclear Engineering, Kyushu University
Motooka 744, Nishi-ku, Fukuoka 819-0395 (Japan)
[f] National Institute of Technology, Numazu College
3600 Ooka, Numazu, Shizuoka 410-8501 (Japan)
[g] Graduate School of Chemical Sciences and Engineering, Hokkaido University, Sapporo 060-0810, Japan
[h] Department of Chemistry, Faculty of Science, Hokkaido University
Sapporo 060-0810, (Japan)
[i] Institute for Chemical Reaction Design and Discovery (WPI-ICReDD), Hokkaido University
Sapporo 001-0021, (Japan)
[j] PRESTO, Japan Science and Technology Agency
Kawaguchi 332-0012, (Japan)

Abstract:

To realize a sustainable, carbon-free society, catalysts for the synthesis of ammonia using renewable energy under mild reaction conditions (<400 °C, <10 MPa) are needed. Ru-based catalysts are currently the most promising candidates; however, Ru is expensive and of low abundance. Here, we discovered that encapsulation of Co nanoparticles with BaO-enhanced the ammonia synthesis activity of the Co, and that a simple Ba-doped Co/MgO catalyst pre-reduced at an unusually high temperature of 700 °C (Co@BaO/MgO-700red) showed outstanding ammonia synthesis activity. The ammonia synthesis rate (24.6 mmol g_{cat}^{-1} h^{-1}) and turnover frequency (0.255 s^{-1}) of the catalyst at 350 °C and 1.0 MPa were 22 and 64 times higher, respectively, than those of the non-doped parent catalyst. At the same temperature but higher pressure (3.0 MPa), the ammonia synthesis rate was increased to 48.4 mmol g_{cat}^{-1} h^{-1}, which is higher than that of active Ru-based catalysts. Scanning transmission electron microscopy and energy dispersive X-ray spectrometry investigations revealed that after reduction at 700 °C the Co nanoparticles had become encapsulated by a nano-fraction of BaO. The mechanism underlying the formation of this unique structure was considered to comprise reduction of oxidic Co to metallic Co, decomposition of $BaCO_3$ to BaO, and migration of BaO to the Co nanoparticle surface. Spectroscopic and density-functional theory investigations revealed that adsorption of N_2 on the Co atoms at the catalyst surface weakened the N_2 triple bond to the strength of a double bond due to electron donation from the Ba atom of BaO *via* adjacent Co atoms; this weakening accelerated cleavage of the triple bond, which is the rate-determining step for ammonia synthesis.

Introduction

Ammonia is an indispensable chemical feedstock in today's society. Currently, more than 80% of the ammonia produced is used as fertilizer for the production of food that feeds almost half of the world's population.[1] Recently, ammonia has attracted attention as a potential carrier and source of renewable energy, which if realized will be important steps toward a sustainable and carbon-free society.[2-6] Currently, most ammonia is synthesized by reaction of nitrogen and hydrogen *via* the Haber–Bosch process. However, the Haber–Bosch process is energy-intensive, requires the consumption of fossil fuels for the production of hydrogen, and produces large amounts of CO_2 (1.9 ton-NH_3^{-1}).[7] Also, the Fe-based catalysts used in the Haber–Bosch process need very high temperatures and pressures (>450 °C, >20 MPa)[8] to activate the nitrogen triple bond (N≡N; bond dissociation energy, 945 kJ mol^{-1}) and to obtain high rates of ammonia synthesis. Thus, to realize a green ammonia synthesis process that uses renewable energy, catalysts that can produce ammonia under mild reaction conditions (<400 °C, <10 MPa) are needed.[9]

Ruthenium (Ru) catalysts are broadly regarded as the most promising candidates for realizing processes for the production of green ammonia.[10-15] However, Ru is relatively rare and therefore expensive. As an alternative to Ru, cobalt (Co) has been suggested because it catalyzes ammonia synthesis and is relatively abundant,[16] but neat Co is less catalytically active than both Ru and Fe due to the small adsorption energy of molecular N_2 on Co.[17] Several strategies to enhance the ammonia synthesis activity of Co have been reported, including addition of alkaline or alkaline earth metals,[18-21] alloying with other transition metals,[19,22,23] and combination with other functional materials.[12,24-29] Among the elements used in these strategies, barium (Ba), an alkaline earth metal, is a well-known promoter of Ru catalysts that has also been reported to enhance the ammonia synthesis activity of Co catalysts. Hagen *et. al.* have reported that Ba addition improves the activity of Co/C catalysts by increasing the number of active sites in the catalyst and lowering the activation energy.[18,19] Lin *et al.* have reported that addition of Ba to Co/CeO_2 catalysts enhances their ammonia synthesis activity.[30] However, despite these efforts, the ammonia synthesis activity of these catalysts remains low under mild reaction conditions. To address this issue, Co catalysts promoted by or loaded on non-oxidic Ba materials, such as BaH_2-Co/carbon nanotubes[24] and Co/Ba-$Ca(NH_2)_2$,[12] have been developed. These catalysts show relatively high ammonia synthesis activity below 400 °C; however, they are difficult to synthesize and are unstable under atmospheric conditions, which has hampered their commercial application. Thus, although metal oxide–supported Co catalysts are easy to prepare and handle compared with non-oxidic Co catalysts, their catalytic activity under mild reaction conditions remains to be improved.

Here, we discovered that encapsulation of Co nanoparticles with BaO as a result of surface rearrangement of the catalyst during reduction at an unusually high temperature enhanced the ammonia synthesis activity of the Co catalyst. Compared with previously reported Co catalysts, our Co/Ba/MgO catalyst (Co@BaO/MgO-700red) showed the highest ammonia synthesis rate per weight of catalyst under mild reaction conditions (350 °C): 24.6 mmol h^{-1} g_{cat}^{-1} at 1.0 MPa and 48.4 mmol g_{cat}^{-1} h^{-1} at 3.0 MPa. In addition, the ammonia synthesis rate of Co@BaO/MgO-700red at 3.0 MPa was higher than that reported for the active Ru-based catalysts.[10,31-33] To clarify how Ba doping affected the catalyst, we performed atomic-scale observations using spherical aberration–corrected scanning transmission electron microscopy (Cs-STEM) coupled with energy dispersive X-ray spectrometry (EDX), X-ray absorption fine structure (XAFS) analysis, and infrared (IR) spectroscopy after N_2 adsorption, and we conducted a density-functional theory analysis. We found that during reduction a nano-fraction of BaO had encapsulated the Co nanoparticles, and that electron donation from the Ba atom of BaO *via* adjacent Co atoms to adsorbed molecular N_2 accelerated activation of $N{\equiv}N$.

Experimental Section

Catalyst preparation. Ba-doped MgO-supported Co catalyst (Co/Ba/MgO) was prepared by a sequential impregnation method. First, a commercial MgO support (MgO-500A, Ube Material Industries, Ltd., Japan) was added to an aqueous solution of $Ba(OH)_2$ (FUJIFILM Wako Pure Chemical Corporation, Japan). The amount of Ba was fixed at Ba/(Ba + Mg) = 0.01 mol/mol. After stirring for 1 h, the aqueous solvent was removed by rotary evaporation. The obtained powder was calcined at 700 °C for 5 h in static air. Next, the support was impregnated with cobalt(II) acetylacetonate hydrate ($Co(acac)_2$) in tetrahydrofuran (both FUJIFILM Wako). The Co loading was fixed at 20 wt% for each catalyst. The mixture of impregnated support and $Co(acac)_2$ was dried in a rotary evaporator, and the obtained powder was heated to 500 °C under an Ar stream and kept at 500 °C for 5 h to remove the ligand from the $Co(acac)_2$. Co/MgO without Ba additive was prepared by using the same procedure as that used to prepare Co/Ba/MgO but excluding the process of impregnation, drying, and calcination of $Ba(OH)_2$. Three benchmark Ru catalysts ($Ru/La_{0.5}Ce_{0.5}O_x$, Ru/CeO_2, and $Cs^+/Ru/MgO$) were also prepared by using the procedure we reported previously.[14,33]

Evaluation of ammonia synthesis activity. Ammonia synthesis activity was evaluated using a conventional flow system under a pressurized atmosphere. In brief, pelleted catalyst was added to a tubular Inconel reactor (The Nilaco Corporation, Japan) and reduced in a flow of pure H_2 at 500 or 700 °C for 1 h at 0.1 MPa and then cooled to 300 °C in an Ar stream. After the pressure was adjusted at 300 °C, a H_2/N_2 mixture [3:1 (mol/mol)] was fed into the reactor. In this report, all of the pressures cited are absolute pressures. The ammonia synthesis rate was determined from the rate of decrease of electron conductivity of a sulfuric acid solution, as monitored with an electron conductivity detector (CM-30R, DKK-TOA, Japan). The detailed test procedure is provided in Supporting Information.

Kinetic analysis. Reaction kinetics were analyzed by using a previously reported method.[34-36] The reaction orders with respect to N_2, H_2, and NH_3 were determined by measuring the N_2, H_2, and NH_3 pressure dependence of the ammonia synthesis rate under assumption of the following rate expression:

$$r = kP_{\mathrm{N_2}}^{n}P_{\mathrm{H_2}}^{h}P_{\mathrm{NH_3}}^{a}$$

Catalyst characterization. High-angle annular dark-field scanning transmission electron microscopy (HAADF-STEM) images and EDX elemental maps were obtained by using Cs-STEM equipped with an EDX detector (JEM-ARM200CF, JEOL, Japan). To investigate the physiochemical properties of the catalysts, specific surface area based on the Brunauer−Emmett−Teller theory and H_2 chemisorption capacity were measured. Infrared spectra of adsorbed N_2 were measured with a spectrometer (FT/IR-6600, JASCO, Japan) equipped with a mercury–cadmium–telluride detector. X-ray diffraction (XRD) analysis was performed with a SmartLab X-ray diffractometer (Rigaku, Japan). XAFS measurements of the Co K-edges were performed on the BL01B1 beamline at SPring-8 (Hyogo, Japan) with the approval of the Japan Synchrotron Radiation Research Institute (Hyogo, Japan). Detailed procedures used in the characterization are described in Supporting Information.

Computational details. To examine the effect of BaO on catalytic activity, density-functional theory calculations were performed for Co_{20}, BaO/Co_{20}, N_2/Co_{20}, and $N_2/BaO/Co_{20}$ by using the TURBOMOLE program[37] using the resolution-of-the-identity approximation, Perdew–Burke–Ernzerhof functional,[38] and the def-SV(P) basis set[4] along with the relativistic effective core potential for Ba.[39] The model of the Co_{20} cluster was assumed to have a tetrahedral geometry with four (111) faces, as we assumed previously for the interaction between NH_3 and Pt or Cu catalysts.[40,41]

Results and Discussion

Ammonia synthesis activity of Co@BaO/MgO-700red.

First, we evaluated the NH_3 synthesis activity of Co@BaO/MgO-700red (Fig. 1). Figure 1a shows the temperature dependence of the ammonia synthesis rates of Co@BaO/MgO-700red, Co/Ba/MgO-500red, and Co/MgO-700red. The ammonia synthesis rate of Co@BaO/MgO-700red was much higher than those of Co/Ba/MgO-500red and Co/MgO-700red across the temperature range examined (150–450 °C). At 350 °C, the ammonia synthesis rate of Co@BaO/MgO-700red (24.6 mmol h^{-1} g_{cat}^{-1}) was around 10 times that of Co/Ba/MgO-500red and around 77 times that of Co/MgO-700red (Table 1). In addition, Co@BaO/MgO-700red showed catalytic activity at temperatures below 300 °C (10.5 mmol h^{-1} g_{cat}^{-1}), whereas the other two catalysts did not. Although a direct comparison of the activity of Co@BaO/MgO-700red with that of previously reported catalysts is difficult because of the different Co loadings, reaction pressures, and space velocities used, the ammonia synthesis activity of Co@BaO/MgO-700red was comparable to or higher than that of other reported Co catalysts (Table S1). Co@BaO/MgO-700red also showed a higher ammonia synthesis rate per weight of catalyst at and below 400 °C than did Co/Ba-$Ca(NH_2)_2$, which is the most active Co catalyst reported to date.[12] Thus, these results clearly showed that Co@BaO/MgO-700red had high catalytic activity, and that this high catalytic activity was a result of doping with Ba and pre-reduction at high temperature.

Figure 1b shows Arrhenius plots for Co@BaO/MgO-700red, Co/Ba/MgO-500red, and Co/MgO-700red. The calculated apparent activation energies were 51.9, 77.5, and 80.4 kJ mol^{-1}, respectively, indicating that doping with Ba and reduction at high temperature decreased the apparent activation energy, which explains the high ammonia synthesis rate of Co@BaO/MgO-700red.

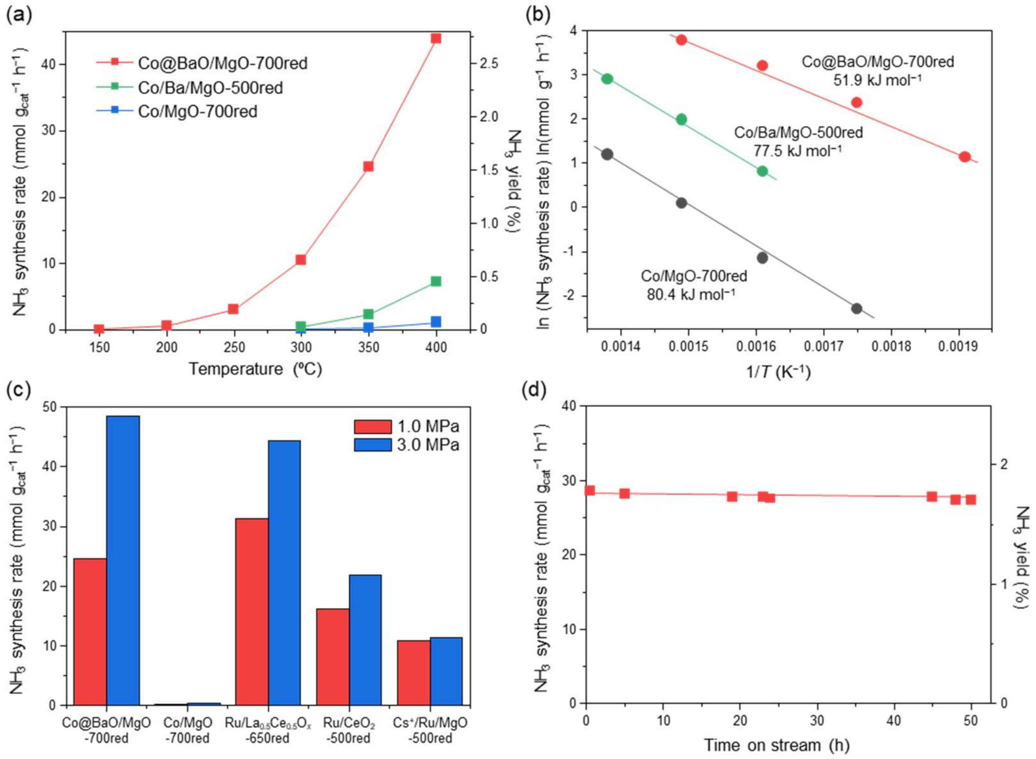

Figure 1. Evaluation of the ammonia (NH_3) synthesis activities of MgO-supported Co catalysts. (a) Temperature dependence of NH_3 synthesis rate and yield at 1.0 MPa. (b) Arrhenius plots for NH_3 synthesis reactions at 1.0 MPa. (c) Ammonia synthesis rate at 350 °C over supported Co or Ru catalysts reduced at the optimal temperature for that catalyst. *xxx*red means the catalyst was pre-reduced at xxx °C. (d) Time course of ammonia formation rate over Co@BaO/MgO-700red at 350 ºC, 1.0 MPa.

Figure 1c shows a comparison of the catalytic activities of Co@BaO/MgO-700red, Co/MgO, and three previously reported Ru catalysts at 350 °C and 1.0 or 3.0 MPa. Under such low temperature, Ru catalyst shows much higher activity than Fe and Co based catalyst.[42] At 1.0 MPa, Co@BaO/MgO-700red showed a higher ammonia synthesis rate compared with that of Cs^+/Ru/MgO, an Ru catalyst often used as a benchmark of ammonia activity,[10,31,43] and that of Ru/CeO_2, which a national project in Japan has suggested is a potential candidate for use in ammonia synthesis processes using renewable energy;[32] however, it had a lower ammonia synthesis rate than that of Ru/$La_{0.5}Ce_{0.5}O_x$, which is one of the most active Ru catalysts reported to date.[33,44] When the reaction pressure was increased to 3.0 MPa, the ammonia synthesis rate of Co@BaO/MgO-700red was markedly increased to 48.4 mmol g_{cat}^{-1} h^{-1}, which was higher than that of the three Ru catalysts. Note that the ammonia synthesis rate of the Ru catalysts did not increase as much as it did for Co@BaO/MgO-700red when the reaction pressure was increased from 1.0 to 3.0 MPa.

To understand more about the underlying causes of the different catalytic behaviors among Co@BaO/MgO-700red and the three Ru catalysts, we performed kinetic analyses at 350 °C (Table S2 and Fig. S1). The reaction order with respect to N_2 was in the range of 0.76–1.07 for all of the catalysts, suggesting that the rate-determining step for ammonia synthesis over each catalyst was dissociation of N≡N. The reaction order with respect to H_2 for the Ru catalysts was in the range of −0.76 to 0.15, which is likely a result of the strong hydrogen adsorption character of Ru. Hydrogen adsorption on the surface of the catalyst can poison the catalyst, reducing its catalytic activity, which is a major drawback for most oxide- or carbon-supported Ru catalysts.[45]. Thus, the low reaction order with respect to H_2 for the Ru catalysts explains the observed moderate increase of ammonia synthesis rate when the reaction pressure was increased from 1.0 to 3.0 MPa (Fig. 1c). In contrast, the reaction order with respect to H_2 for Co@BaO/MgO-700red was 0.37, indicating that this catalyst is free from hydrogen poisoning, which explains the large increase in ammonia synthesis activity observed for this catalyst when the reaction pressure was increased (Fig. 1c). Together, these results demonstrate that Co@BaO/MgO-700red has the potential to replace Ru catalysts for ammonia synthesis under mild reaction conditions. The high ammonia synthesis rate over Co@BaO/MgO-700red remained stable for 50 h at 350 °C and 1.0 MPa (Fig. 1d), demonstrating the long-term stability of Co@BaO/MgO-700red.We also compared the ammonia synthesis activity of Co@BaO/MgO-700red with that of a commercial wüstite-based fused iron catalyst (AmoMax 10RS, Clariant, Japan) (400 °C, 0.1–6.0 MPa). The ammonia synthesis rate of Co@BaO/MgO-700red increased linearly from 5.6 to 141 mmol h^{-1} g_{cat}^{-1} as the pressure was increased from 0.1 to 6.0 MPa and was higher than that of the commercial fused iron catalyst at all pressures examined (Fig. S2). The difference in activity between the two catalysts was more pronounced at higher pressures. These results indicate the potential of using Co@BaO/MgO-700red to replace Fe-based catalysts for the industrial production of ammonia *via* the Haber–Bosch process.

Influence of Ba on the ammonia synthesis activity of MgO-supported Co catalysts

To elucidate the effect of doping with Ba on the ammonia synthesis activity of the Co catalyst, we first compared the physicochemical properties of Co/MgO catalysts reduced at 700 °C with or without Ba doping (Table 1). Co@BaO/MgO-700red (Entry 1) had a slightly smaller specific surface area than did Co/MgO-700red (Entry 3), and the Co particles of Co@BaO/MgO-700red were slightly larger than those of Co/MgO-700red. However, Co@BaO/MgO-700red had an H_2 chemisorption capacity that was one-third that of Co/MgO-700red. Furthermore, the turnover frequency of Co@BaO/MgO-700red was more than 60 times greater than that of Co/MgO-700red. Together, these results indicate that Ba has strong structural and chemical interactions with Co that result in a catalyst with a small number of highly active Co sites for ammonia synthesis.

Table 1. Physicochemical properties and catalytic performance of supported Co catalysts

Entry	Catalyst	SSA[a] [$m^2\ g_{cat}^{-1}$]	H_2 chemisorption [b] [$\mu mol\ g_{cat}^{-1}$]	d[c] [nm]	Rate[d] [$mmol\ g_{cat}^{-1}\ h^{-1}$]	TOF[e] [s^{-1}]	Fraction of Co^0[f] [at.%]
1	Co@BaO/MgO-700red	42.0	13.9	10.6 ± 3.4	24.6	0.255	92.6
2	Co/Ba/MgO-500red	61.9	24.6	6.3 ± 1.0	2.3	0.013	71.4
3	Co/MgO-700red	47.6	42.6	7.6 ± 1.2	1.1	0.004	78.9

[a] Specific surface area.

[b] Dispersion estimated from the H_2 chemisorption capacity.

[c] Mean diameter of Co nanoparticles estimated by transmission electron microscopy.

[d] Ammonia synthesis rate at 350 ºC and 1.0 MPa.

[e] Turnover frequency. Calculated from the H_2 chemisorption value and the NH_3 synthesis rate shown in Table 1.

[f] Estimated by linear combination analysis of Co K-edge X-ray absorption near edge structure spectra.

Next, we performed an XAFS analysis to investigate how Ba doping changed the state and local structure of Co in the catalyst. Co K-edge XANES spectra for Co/Ba/MgO and Co/MgO are shown in Figure 2 together with the spectra for several reference samples. The spectrum for as-prepared Co/Ba/MgO (spectrum f) and Co/MgO (spectrum i) was comparable with that of CoO, suggesting that the valence of Co in the catalyst was +2, as it is in the Co precursor, $Co(acac)_2$. After reduction of the catalyst at 700 °C, the peaks shifted to a lower energy, and a characteristic pre-edge peak at 7707 eV was observed (spectra h and j), indicating that the Co^{2+} in Co/Ba/MgO and Co/MgO were reduced to the metallic state. Linear combination of the Co K-edge XANES spectra of CoO and Co foil indicated that the degree of reduction of Co in Co@BaO/MgO-700red and Co/MgO-700red was 93% and 78%, respectively. These results indicate that oxidic Co, which contains an electron-withdrawing oxygen atom, is reduced to metallic Co during reduction and that the addition of Ba promoted this reduction of oxidic Co.

The k^3-weighted extended XAFS (EXAFS) spectra and their Fourier transforms (FTs) for the catalysts and reference samples are shown in Figure S3, and curve fitting results for the catalysts are summarized in Table S3. The FT EXAFS spectra for the as-prepared Co catalysts were comparable with the spectrum for CoO. However, the FT EXAFS spectra of Co/MgO-700red and Co@BaO/MgO-700red were comparable with those for metallic Co, including a small contribution from CoO. These results are consistent with the results obtained from the XANES spectra. The FTs of Co@BaO/MgO-700red and Co/MgO-700red both showed a peak at 2.48–2.49 Å that was assigned to the Co−Co bond. Curve fitting revealed that the coordination number of Co−Co bonds for Co@BaO/MgO-700red was 10.7 ± 0.5 and for Co/MgO-700red was 9.0 ± 0.5 (Table S3), suggesting that the Co nanoparticles in Co@BaO/MgO-700red were slightly larger than those in Co/MgO-700red, which is consistent with our STEM observations (Table 1).

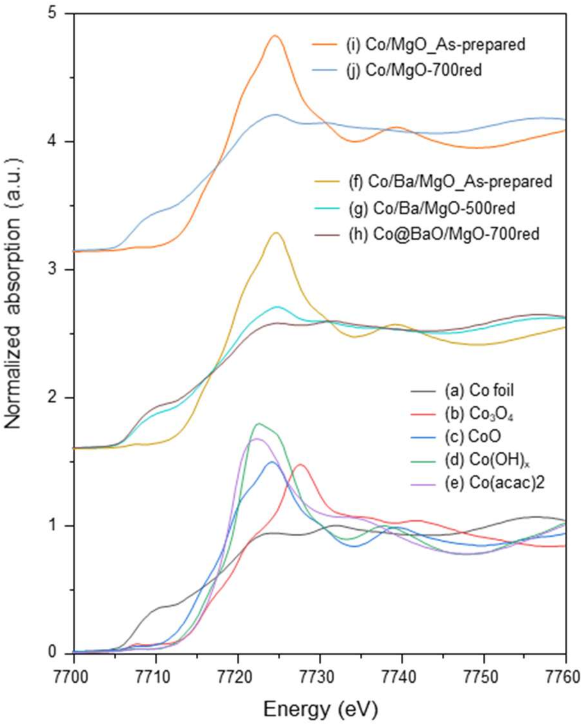

Figure 2. Normalized Co K-edge X-ray absorption near-edge structure spectra for as-prepared and reduced Co/MgO and Co/Ba/MgO catalysts, and for reference samples. *xxx*red means the catalyst was pre-reduced at xxx °C.

We also examined the surface structure of Co@BaO/MgO-700red by Cs-STEM observation and elemental distribution mapping (Fig. 3). To avoid exposure of the sample to the air, we used a special STEM holder with a gas cell to transfer the catalyst sample from an inert gas environment to the inside of the STEM column.[14,33] EDX elemental maps showed that Ba was localized around the Co nanoparticles (Fig. 3b–e). In addition, high-resolution, high-magnification HAADF-STEM images clearly showed that the Co nanoparticles were encapsulated within low-crystalline nano-fractions of Ba compounds (Fig. 3a, f, g). These results are interesting because during preparation of the catalyst the Ba was loaded to the MgO support before the Co precursor, meaning that the encapsulation of the Co nanoparticles occurred during reduction. This encapsulation likely explains the much lower H_2 chemisorption observed for Co@BaO/MgO-700red than for Co/MgO-700red (Table 1). Thus, we attributed the high catalytic activity of Co@BaO/MgO-700red to highly active Co nanoparticles contacting with nano-fractions of Ba compounds with low electronegativity.

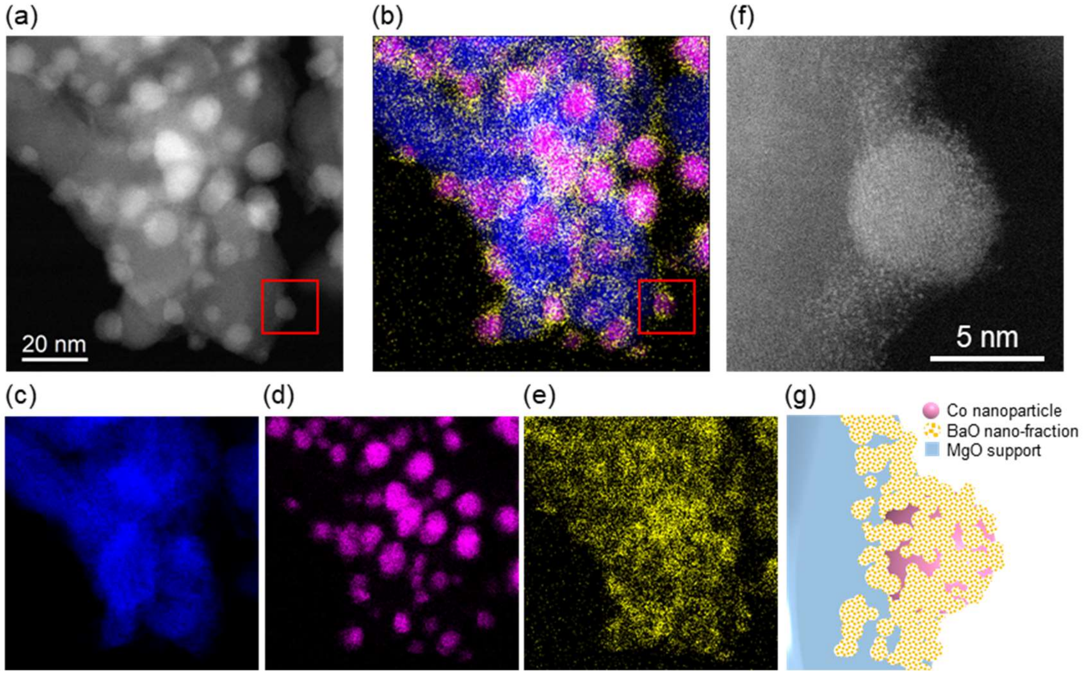

Figure 3. High-angle annular dark-field scanning transmission electron microscopy (HAADF-STEM) images and energy dispersive X-ray (EDX) maps of Co@BaO/MgO-700red without exposure to air. (a) HAADF-STEM image. (b) Overlay EDX map. (c) Mg K. (d) Co K. (e) Ba L. (f) HAADF-STEM image of the area indicated by the red square in (a) and (b). (g) Schematic representation of the surface structure of Co@BaO/MgO-700red.

Next, we investigated the influence of Ba on the activation (i.e., cleavage) of N≡N by means of Fourier transform infrared (FT-IR) spectroscopy of $^{14}N_2$ or $^{15}N_2$ before and after adsorption on Co/MgO-700red or Co@BaO/MgO-700red at −140 °C (Fig. 4a). Ohnishi *et al*. have reported that the stretching vibration mode of molecular $^{14}N_2$ adsorbed on the Co atom of Co/Al_2O_3 is attributable to a peak at 2214 cm^{-1}.[46] The FT-IR spectra for $^{14}N_2$ adsorbed on Co/MgO-700red showed a sharp peak at 2179 cm^{-1}, which is slightly lower than the value reported by Ohnishi *et al*. When $^{15}N_2$ was adsorbed, a peak at an even lower wave number (2107 cm^{-1}) was observed; however, this wave number is in good agreement with the value estimated by considering the isotopic labeling effect ($2179 \times (14/15)^{1/2} = 2105$ cm^{-1}).[47,48] Thus, these two peaks were attributed to N_2 adsorbed on Co. In contrast, the FT-IR spectra for Co@BaO/MgO-700red showed a broad, shallow peak at 1813 cm^{-1} for $^{14}N_2$ and at 1755 cm^{-1} for $^{15}N_2$, and we confirmed that these peaks are assignable to molecular N_2 by considering the isotopic labeling effect ($1813\ cm^{-1} \times (14/15)^{1/2} = 1751\ cm^{-1}$). The peaks for Co@BaO/MgO-700red were at a much lower wave number than the peaks for Co/MgO-700red, indicating that the N≡N bond of N_2 adsorbed on Co@BaO/MgO-700red was markedly weakened by the presence of Ba compounds.

To study the influence of Ba on the electronic state of Co at the atomic scale, we used density-functional theory calculations to estimate the natural charge of the Co atoms in a tetrahedral Co_{20} cluster (four fcc-(111) faces) associated with one BaO molecule. In the initial structure, the Ba atom was placed above the center of one of the 111 faces. The optimized structure of the BaO/Co_{20} system is given in Figure 4b. Note that the state of the Ba compounds in the catalyst was clarified in later analyses to be BaO. The charges of each of the Ba, O, and Co atoms are shown in Figure S5 together with a ball-and-stick representation of the optimized structure with a color overlay of atomic charge. Figure 4c shows a summary of the data shown in Figure S5. Assuming that the total charge of the BaO/Co_{20} cluster is neutral, the total positive charge of BaO (+0.18; sum of Ba (+1.33) and O (−1.15)) indicates that an electron is transferred from the Ba^{2+} of BaO to the Co_{20} cluster. The two Co atoms (Co4 and 5 in Fig. 1c) bonded with the O atom and to Co1 were strongly positively charged. In contrast, the Co atom closest to the Ba atom (Co1) was strongly negatively charged, indicating electron donation from the Ba atom. The remaining seven Co atoms bonded to Co1 (Co2, 3, 6, 7, 14, 15, and 16) were also negatively charged but to different degrees, which can be explained by the Ba atom being offset from the center of the face. The remaining Co atoms in the cluster had almost a neutral charge. Together, these results clearly indicate that an electron is transferred from BaO to the Co cluster, and that the charge transfer is largest around the Ba atom but then decreases with increasing distance from the Ba atom.

To examine how the presence of BaO affects N_2 adsorption on the Co_{20} cluster, we performed geometry optimizations for N_2/Co_{20} (Fig. S6) and $N_2/BaO/Co_{20}$ (Fig. S7). For BaO/Co_{20}, in most optimized structures starting by placing N_2 on the same face to BaO, N_2 was generally adsorbed on the Co atoms adjacent to the Ba atom. A two-dimensional plot of wave number and intensity of stretching vibration of N_2 on Co_{20} (blue) or BaO/Co_{20} (red), estimated by density-functional theory analysis, is shown in Figure 4d. Irrespective of the presence or absence of BaO, a red shift (shift to a lower wave number) of the vibrational frequency for the N≡N stretching mode was observed upon adsorption of N_2 to the cluster. However, the red shift was larger for side-on than for end-on configurations for both N_2/Co_{20} and $N_2/BaO/Co_{20}$. End-on adsorption to a bridge site showed a red shift that was larger than that for atop configuration. When N_2 was adsorbed in the same configuration on Co_{20} and BaO/Co_{20}, the wave number was shifted lower for BaO/Co_{20} than it was for Co_{20} due to electron donation from BaO to N_2 *via* Co. The intensity of N_2 stretching mode decreased with decreasing wave number, probably due to weaker polarization of adsorbed N_2. In addition, the Wiberg bond index[49] of N_2 adsorbed on Co_{20} was around 1.9 to 2.4 and around 1.2 to 1.8 for end-on and side-on configurations, respectively; the Wiberg bond index of N_2 adsorbed on BaO/Co_{20} showed a similar red shift for different configurations, but the values were smaller than those for Co_{20}, indicating that N≡N is weakened upon adsorption to the cluster and that this weakening of the bond is facilitated in the presence of BaO.

Note that the calculated wave number of adsorbed N_2 on Co_{20} with end-on configuration was 1823 to 2146 cm^{-1} (Fig. S6), which is in agreement with the wave number obtained by IR measurement of Co/MgO-700red (2179 cm^{-1}). Furthermore, the calculated wave number of adsorbed N_2 on negatively charged Co atoms in BaO/Co_{20} with end-on configuration was 1652 to 1980 cm^{-1}, which is in agreement with the wave number obtained by IR measurement of Co@BaO/MgO-700red (1813 cm^{-1}) (Fig. 4a). These results indicate that N_2 is adsorbed on Co@BaO/MgO-700red and Co/MgO-700red in an end-on orientation and that an electron is strongly donated to the antibonding π-orbitals of the N≡N bond from BaO via adjacent Co atoms. Furthermore, the triple bond of molecular N_2 adsorbed on Co@BaO/MgO-700red seems to be weakened to about the strength of a double bond because the Wiberg Bond Index is estimated to be around 1.6 to 2.1. To the best of our knowledge, this is the first spectroscopic and theoretical evidence that Ba works as an "electronic promoter" in a Co-based ammonia synthesis catalyst.

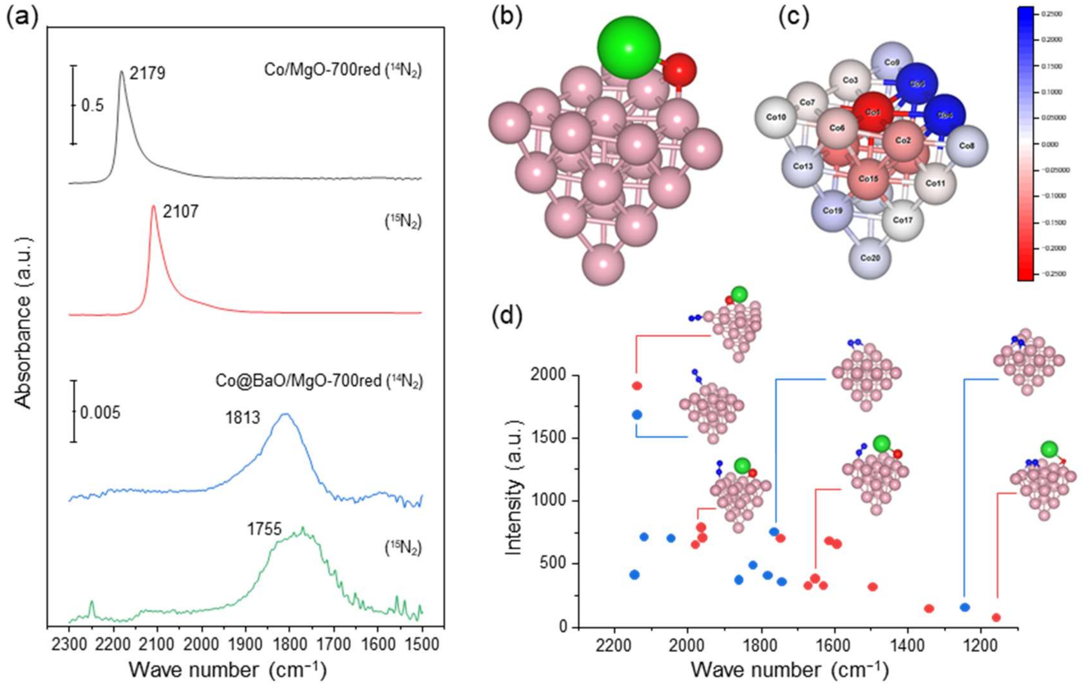

Figure 4. Fourier transform infrared spectra of N_2 and density-functional theory analysis. (a) Infrared spectra of N_2 before and after adsorption on Co/MgO-700red and Co@BaO/MgO-700red. (b) Optimized structure of the BaO/Co_{20} cluster. (c) Optimized structure of the BaO/Co_{20} cluster with a color overlay of atomic charge. (d) Two-dimensional plot of the N≡N stretching mode for N_2/Co_{20} (blue) and N_2/BaO/Co_{20} (red), with the x- and y-axes showing the wave number and intensity of the N_2 stretching mode, respectively. The complete sets of optimized structures are shown in Figures S6 and S7.

Influence of high-temperature reduction on catalytic properties. As already discussed, we found that the ammonia synthesis rate of Co/Ba/MgO was increased by increasing the reduction temperature from 500 to 700 °C (Fig. 1). We therefore investigated the effect of reduction temperature on the physiochemical properties and structure of the catalyst (Table 1, Entries 1 and 2). When the reduction temperature was increased from 500 to 700 °C, the specific surface area was decreased from 61.9 to 42.0 $m^2\ g_{cat}^{-1}$. The mean diameter of Co particles was increased from 6.3 to 10.6 nm, indicating that the higher temperature induced sintering of the catalyst. At the same time, the H_2 chemisorption value decreased from 24.6 to 13.9 μmol g_{cat}^{-1}, meaning that the number of available Co sites was decreased by reduction at the higher temperature. In contrast, turnover frequency drastically increased from 0.013 to 0.255 with the increase in reduction temperature.

To understand why the turnover frequency increased with the increase in reduction temperature, we characterized the two catalysts by using several analysis methods. The degree of Co reduction estimated by linear combination of the Co K edge XANES spectra of CoO and Co foil was 71.4% and 92.6% for Co/Ba/MgO-500red and Co@BaO/MgO-700red, respectively, indicating that reduction at high temperature is essential to reduce inactive oxidic Co to active metallic Co (Fig.

2). The coordination number of Co−Co bonds for Co/Ba/MgO-500red and Co@BaO/MgO-700red was 8.1 ± 0.6 and 10.7 ± 0.5, respectively (Table S3), indicating that the Co nanoparticles were sintered during the high-temperature reduction, which is consistent with our Cs-STEM observations (Table 1 and Fig. S4).

To understand the localization of each element in Co/Ba/MgO catalyst, we carried out elemental mapping and Cs-STEM observation of the catalyst after exposure to air following reduction at 500 or 700 °C (Fig. 5). For Co/Ba/MgO-500red, Ba was distributed throughout the catalyst (Fig. 5a). XRD analysis of the catalyst revealed that the crystal structures of MgO and $BaCO_3$ were periclase–type and witherite-type, respectively (Fig. S7). No peak shifts or peaks attributable to a composite of MgO and Ba species were observed. In contrast, for Co@BaO/MgO-700red, sintering of the MgO grains and Co nanoparticles was observed, and Ba was enriched on the surface of both sintered materials, particularly on the surface of the Co nanoparticles and at the Co/MgO interface. (Fig. 5b), indicating that Ba compounds encapsulated the Co nanoparticles. Thus, reduction at 700 °C, but not at 500 °C, resulted not only in sintering of the support and catalyst but also rearrangement of Ba compounds on the catalyst surface.

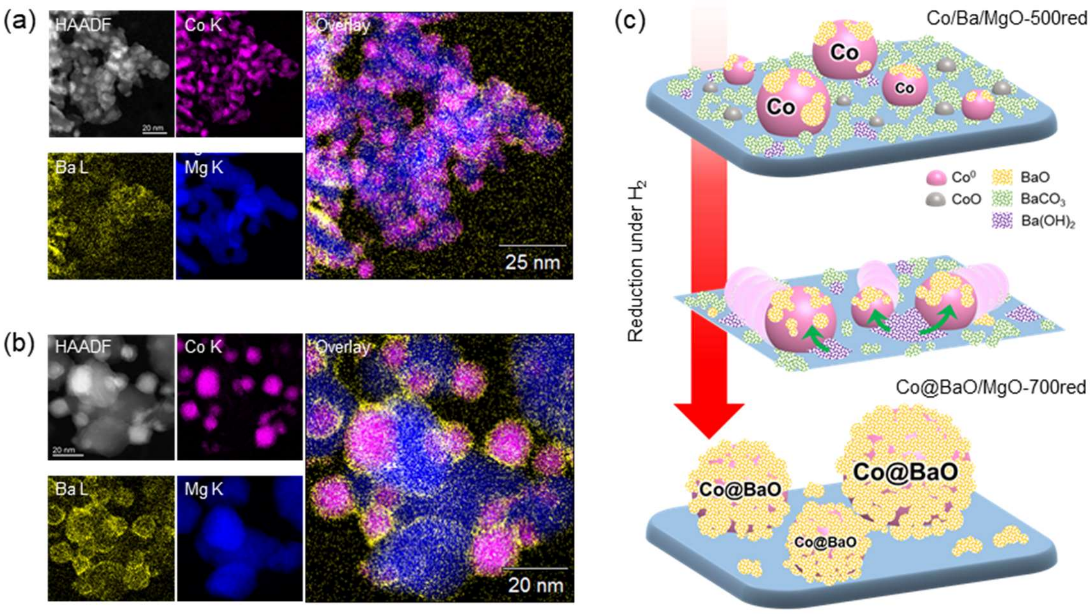

Figure 5. High-angle annular dark-field (HAADF) scanning transmission electron microscopy images and energy dispersive X-ray spectrometry maps of (a) Co/Ba/MgO-500red and (b) Co@BaO/MgO-700red. (c) Schematic illustration of the formation of the surface structure of Co@BaO/MgO-700red during reduction to 700 °C.

To understand how reduction influenced the state of the Ba and Mg compounds in Co/Ba/MgO, we measured IR spectra of as-prepared catalyst and of catalyst after reduction at 500 or 700 °C (Fig. 6). As-prepared Co/Ba/MgO showed characteristic peaks assignable to $Ba(OH)_2$ (2814 cm^{-1}),[50,51] $BaCO_3$ (2447, 1748, 1443, and 1058 cm^{-1}),[51] and $MgCO_3$ (1555 cm^{-1}). A broad peak at 3750 to 2500 cm^{-1} was assigned to water moisture adsorbed on the catalyst surface. After reduction at 500 °C, only the peaks attributed to $BaCO_3$ (1748 and 1443 cm^{-1}) and $MgCO_3$ (1555 cm^{-1}) were observed. After reduction at 700 °C, the four peaks assigned to $BaCO_3$ and the peak assigned to $MgCO_3$ were not observed, indicating that reduction at high temperature (i.e., 700 °C), but not at low temperature (i.e., 500 °C), was needed to completely remove carbonates from the catalyst. Similar results were obtained by XRD analysis (Fig. S3), where as-prepared Co/Ba/MgO and Co/Ba/MgO-500red showed small diffraction peaks assignable to $BaCO_3$. The presence of carbonate decreases the electron-donating ability of the support material; therefore, we concluded that one of the reasons for the enhanced turnover frequency of the catalyst reduced at 700 °C was complete decomposition of $BaCO_3$ and $MgCO_3$ by hydrogen and the formation of BaO and MgO, which have strong electron-donating ability.

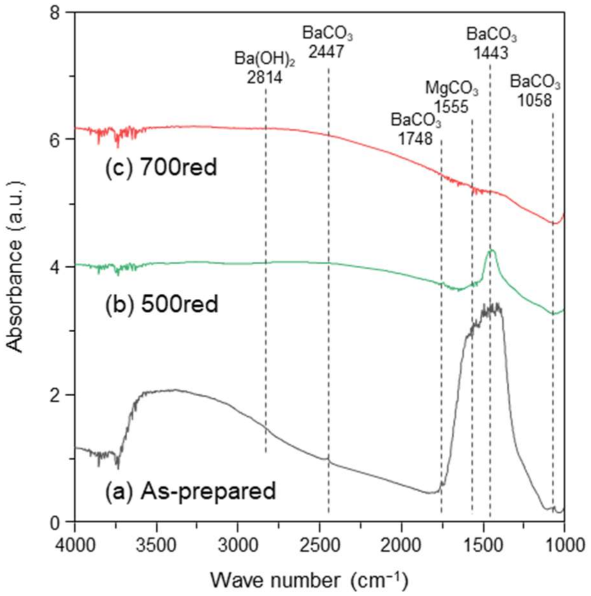

Figure 6. Infrared spectra for Co/Ba/MgO before and after reduction at 500 or 700 °C.

Surface rearrangement and construction of the active sites in Co@BaO/MgO-700red during reduction. Finally, we considered the formation of the surface structure of Co@BaO/MgO-700red during reduction at high temperature (Fig. 5c). As already discussed, a major part of the Ba in the as-prepared catalyst was found to exist as $BaCO_3$. The $BaCO_3$ were decomposed only partly by reduction at 500 ºC but were fully decomposed by reduction at 700 ºC by hydrogen activated on the Co nanoparticles. The decomposition reaction of $BaCO_3$ proceeds as follows resulting in the production of BaO:

$$BaCO_3 + 4H_2 \rightarrow BaO + CH_4 + 2H_2O$$

During the decomposition of $BaCO_3$, $Ba(OH)_2$ may be formed and is decomposed to BaO. Ba compounds generally have lower melting points than their Mg counterparts, so the Ba compounds are able to move across the catalyst surface during reduction at high temperature (Table S4). In addition, Ba compounds have low affinity for Mg compounds because both have basic properties. Such low affinity likely drives the migration of Ba compounds over the Co nanoparticles. The Co nanoparticles, in which Co oxide is reduced to metallic Co during reduction, also move across the support surface, come into contact with one another, and become sintered. Meanwhile, Co nanoparticles collect the Ba compounds due to their strong affinity for one another, which leads to the formation of Co nanoparticles encapsulated by a nano-fraction of BaO. In particular, $Ba(OH)_2$, which has a low melting point (408 °C), is liquefied $Ba(OH)_2$ and also migrates to the surface of Co nanoparticles, where it decomposes to BaO, which has a high melting point (1920 °C); the BaO then quickly coagulates as a nano-fraction with an internal void through which gases can pass. Such a unique structure allows for exceptional electron donation from BaO *via* adjacent Co atoms to adsorbed N_2, which strongly promotes cleavage of the N≡N bond.

Conclusions

Here, we report that encapsulation of Co nanoparticles with BaO markedly enhanced the ammonia synthesis activity of Co catalyst. The developed Co@BaO/MgO catalyst showed higher activity than the Co-based catalysts currently reported in the literature and other active Ru catalysts under mild reaction conditions. We experimentally and theoretically clarified that strong electron donation from BaO to surface Co atoms is the key factor in activating the N≡N bond, which is the rate-determining step for ammonia synthesis, although this strong electron donation was found to be limited to a very short range atomically. Therefore, to maximize the effect of BaO, it is essential to place the Ba atom as close as possible to the Co atoms. We found that this could be achieved by H_2 reduction of the catalyst at an unusually high temperature, which resulted in surface rearrangement and the formation of BaO-encapsulated Co nanoparticles on the catalyst surface in which all of the surface-available Co sites were adjacent to nano-fractions of BaO. Our findings are expected to be useful for the development of an innovative, cost-effective, and practical catalyst for the synthesis of green ammonia under mild conditions, which is an important step toward the realization of a sustainable and carbon-free society.

Author Contributions

K.N. designed and K.S. coordinated this project. S. Miyahara, K.T., Y.W. prepared the catalysts, performed the characterizations, and tested catalytic activities. K.I. performed the catalytic activity tests under high-pressure conditions. K.S. conducted FT-IR and XAFS measurements and analyzed the data. T. Toriyama, T.Y., and S. Matsumura conducted Cs-STEM observations and measured EDX spectra. H.M., T.I., and T. Taketsugu conducted DFT calculations. All the authors discussed the results and commented on the study. K.S., K.I., T.I., and K.N. co-wrote the manuscript.

Acknowledgement

This research was supported by a grant from the CREST, JST program (No. JPMJCR1341). Part of this research was financially supported by the TOYOTA Mobility Foundation and the Japan Society for the Promotion of Science (JSPS) KAKENHI Grant No. 20H02522. T.I. is grateful for the financial support provided by JSPS KAKENHI Grant Nos. 20K05412, 20H04652, and

20K05592, and by the PRESTO, JST program (No. JPMJPR20T1). Cs-STEM observations were performed as part of a program conducted by the Advanced Characterization Nanotechnology Platform Japan, sponsored by the Ministry of Education, Culture, Sports, Science and Technology (MEXT), Japan (No. JPMXP09-A-18-KU-0283). X-ray absorption measurements were performed at the BL01B1 facilities of SPring-8 at the Japan Synchrotron Radiation Research Institute (JASRI) (No. 2018B1345). This work was also partly supported by the Elements Strategy Initiative (ESICB) of MEXT (Grant No. JP- MXP0112101003).

References

1 Erisman, J. W., Sutton, M. A., Galloway, J., Klimont, Z. & Winiwarter, W. How a century of ammonia synthesis changed the world. *Nat. Geosci.* **1**, 636-639, doi:10.1038/ngeo325 (2008).

2 Giddey, S., Badwal, S. P. S., Munnings, C. & Dolan, M. Ammonia as a Renewable Energy Transportation Media. *ACS Sustainable Chem. Eng.* **5**, 10231-10239, doi:10.1021/acssuschemeng.7b02219 (2017).

3 Eguchi, K. in *Energy Technology Roadmaps of Japan* (eds Yukitaka Kato, Michihisa Koyama, Yasuhiro Fukushima, & Takao Nakagaki) (Springer Japan, 2016).

4 Schüth, F., Palkovits, R., Schlögl, R. & Su, D. S. Ammonia as a possible element in an energy infrastructure: catalysts for ammonia decomposition. *Energy Environ. Sci.* **5**, 6278-6289, doi:10.1039/c2ee02865d (2012).

5 Klerke, A., Christensen, C. H., Nørskov, J. K. & Vegge, T. Ammonia for hydrogen storage: challenges and opportunities. *J. Mater. Chem.* **18**, 2304-2310, doi:10.1039/b720020j (2008).

6 MacFarlane, D. R. *et al.* A Roadmap to the Ammonia Economy. *Joule* **4**, 1186-1205, doi:10.1016/j.joule.2020.04.004 (2020).

7 Foster, S. L. *et al.* Catalysts for nitrogen reduction to ammonia. *Nat. Catal.* **1**, 490-500, doi:10.1038/s41929-018-0092-7 (2018).

8 Smith, C., Hill, A. K. & Torrente-Murciano, L. Current and future role of Haber–Bosch ammonia in a carbon-free energy landscape. *Energy Environ. Sci.* **13**, 331-344, doi:10.1039/c9ee02873k (2020).

9 Sato, K. & Nagaoka, K. Boosting Ammonia Synthesis under Mild Reaction Conditions by Precise Control of the Basic Oxide–Ru Interface. *Chem. Lett.*, doi:10.1246/cl.200855 (2021).

10 Aika, K. Role of alkali promoter in ammonia synthesis over ruthenium catalysts—Effect on reaction mechanism. *Catal. Today* **286**, 14-20, doi:10.1016/j.cattod.2016.08.012 (2017).

11 Hattori, M., Iijima, S., Nakao, T., Hosono, H. & Hara, M. Solid solution for catalytic ammonia synthesis from nitrogen and hydrogen gases at 50 degrees C. *Nat. Commun.* **11**, 2001, doi:10.1038/s41467-020-15868-8 (2020).

12 Kitano, M. *et al.* Self-organized Ruthenium-Barium Core-Shell Nanoparticles on a Mesoporous Calcium Amide Matrix

for Efficient Low-Temperature Ammonia Synthesis. *Angew. Chem. Int. Ed.* **57**, 2648-2652, doi:10.1002/anie.201712398 (2018).

13 Hattori, M. *et al.* Enhanced Catalytic Ammonia Synthesis with Transformed BaO. *ACS Catal.* **8**, 10977-10984, doi:10.1021/acscatal.8b02839 (2018).

14 Sato, K. *et al.* Surface Dynamics for Creating Highly Active Ru Sites for Ammonia Synthesis: Accumulation of a Low-Crystalline, Oxygen-Deficient Nanofraction. *ACS Sustainable Chem. Eng.* **8**, 2726-2734, doi:10.1021/acssuschemeng.9b06299 (2020).

15 Marakatti, V. & Gaigneaux, E. Recent Advances in Heterogeneous Catalyst for Ammonia Synthesis. *ChemCatChem*, doi:10.1002/cctc.202001141 (2020).

16 Chirik, P. & Morris, R. Getting Down to Earth: The Renaissance of Catalysis with Abundant Metals. *Acc Chem Res* **48**, 2495, doi:10.1021/acs.accounts.5b00385 (2015).

17 Vojvodic, A. *et al.* Exploring the limits: A low-pressure, low-temperature Haber–Bosch process. *Chem. Phys. Lett.* **598**, 108-112, doi:10.1016/j.cplett.2014.03.003 (2014).

18 Hagen, S. *et al.* New efficient catalyst for ammonia synthesis: barium-promoted cobalt on carbon. *Chem Commun (Camb)*, 1206-1207, doi:10.1039/b202781j (2002).

19 Hagen, S. *et al.* Ammonia synthesis with barium-promoted iron-cobalt alloys supported on carbon. *J. Catal.* **214**, 327-335, doi:10.1016/S0021-9517(02)00182-3 (2003).

20 Rarogpilecka, W. *et al.* Carbon-supported cobalt catalyst for ammonia synthesis: Effect of preparation procedure. *J. Catal.* **237**, 207-210, doi:10.1016/j.jcat.2005.10.029 (2006).

21 Kojima, R. & Aika, K. Cobalt molybdenum bimetallic nitride catalysts for ammonia synthesis. *Appl. Catal., A* **219**, 157-170, doi:10.1016/s0926-860x(01)00678-0 (2001).

22 Kojima, R. & Aika, K. Cobalt Molybdenum Bimetallic Nitride Catalysts for Ammonia Synthesis. *Chem. Lett.* **29**, 514-515, doi:10.1246/cl.2000.514 (2000).

23 Kojima, R. & Aika, K. Cobalt Rhenium Binary Catalyst for Ammonia Synthesis. *Chem. Lett.* **29**, 912-913, doi:10.1246/cl.2000.912 (2000).

24 Gao, W. *et al.* Barium Hydride-Mediated Nitrogen Transfer and Hydrogenation for Ammonia Synthesis: A Case Study of Cobalt. *ACS Catal.* **7**, 3654-3661, doi:10.1021/acscatal.7b00284 (2017).

25 Gong, Y. *et al.* Ternary intermetallic LaCoSi as a catalyst for N_2 activation. *Nat. Catal.*, doi:10.1038/s41929-017-0022-0 (2018).

26 Kitano, M. *et al.* Low-Temperature Synthesis of Perovskite Oxynitride-Hydrides as Ammonia Synthesis Catalysts. *J. Am. Chem. Soc.* **141**, 20344-20353, doi:10.1021/jacs.9b10726 (2019).

27 Lu, Y. *et al.* Synthesis of Rare-Earth-Based Metallic Electride Nanoparticles and Their Catalytic Applications to Selective Hydrogenation and Ammonia Synthesis. *ACS Catal.* **8**, 11054-11058, doi:10.1021/acscatal.8b03743 (2018).

28 Wang, X. *et al.* Insight into dynamic and steady-state active sites for nitrogen activation to ammonia by cobalt-based catalyst. *Nat. Commun.* **11**, 653, doi:10.1038/s41467-020-14287-z (2020).

29 Peng, X. *et al.* N-Induced Electron Transfer Effect on Low-Temperature Activation of Nitrogen for Ammonia Synthesis

over Co-Based Catalysts. *ACS Sustainable Chem. Eng.*, doi:10.1021/acssuschemeng.0c05491 (2021).

30 Lin, B. *et al.* Effect of barium and potassium promoter on Co/CeO_2 catalysts in ammonia synthesis. *J.Rare Earths* **36**, 703-707, doi:10.1016/j.jre.2018.01.017 (2018).

31 Javaid, R., Matsumoto, H. & Nanba, T. Influence of Reaction Conditions and Promoting Role of Ammonia Produced at Higher Temperature Conditions in Its Synthesis Process over Cs-Ru/MgO Catalyst. *ChemistrySelect* **4**, 2218-2224, doi:10.1002/slct.201803813 (2019).

32 Nanba, T. *et al.* Explorative Study of a Ru/CeO₂ Catalyst for NH₃ Synthesis from Renewable Hydrogen and Demonstration of NH₃ Synthesis under a Range of Reaction Conditions. *J. Jpn. Petrol. Inst.* **64**, 1-9, doi:10.1627/jpi.64.1 (2021).

33 Ogura, Y. *et al.* Efficient ammonia synthesis over a Ru/La0.5Ce0.5O1.75 catalyst pre-reduced at high temperature. *Chem. Sci.* **9**, 2230-2237, doi:10.1039/c7sc05343f (2018).

34 Aika, K., Kubota, J., Kadowaki, Y., Niwa, Y. & Izumi, Y. Molecular sensing techniques for the characterization and design of new ammonia catalysts. *Appl. Surf. Sci.* **121-122**, 488-491, doi:10.1016/s0169-4332(97)00343-7 (1997).

35 Kojima, R. & Aika, K.-i. Cobalt molybdenum bimetallic nitride catalysts for ammonia synthesis. *Appl. Catal., A* **218**, 121-128, doi:10.1016/s0926-860x(01)00626-3 (2001).

36 Imamura, K. *et al.* Kinetics of ammonia synthesis over Ru/Pr2O3. *J. Taiwan Inst. Chem. Eng.* **105**, 50-56, doi:10.1016/j.jtice.2019.10.006 (2019).

37 Balasubramani, S. G. *et al.* TURBOMOLE: Modular program suite for ab initio quantum-chemical and condensed-matter simulations. *J Chem Phys* **152**, 184107, doi:10.1063/5.0004635 (2020).

38 Perdew, J. P., Burke, K. & Ernzerhof, M. Generalized Gradient Approximation Made Simple [Phys. Rev. Lett. 77, 3865 (1996)]. *Phys. Rev. Lett.* **78**, 1396-1396, doi:10.1103/PhysRevLett.78.1396 (1997).

39 Andrae, D., Huermann, U., Dolg, M., Stoll, H. & Preu, H. Energy-adjustedab initio pseudopotentials for the second and third row transition elements. *Theoret. Chim. Acta* **77**, 123-141, doi:10.1007/bf01114537 (1990).

40 Hinokuma, S. *et al.* Ammonia-rich combustion and ammonia combustive decomposition properties of various supported catalysts. *Catal. Commun.* **123**, 64-68, doi:10.1016/j.catcom.2019.02.005 (2019).

41 Kiritoshi, S. *et al.* Supported binary CuOx–Pt catalysts with high activity and thermal stability for the combustion of NH3 as a carbon-free energy source. *RSC Adv.* **8**, 41491-41498, doi:10.1039/c8ra07969b (2018).

42 Ozaki, A., Aika, K. & Hori, H. A New Catalyst System for Ammonia Synthesis. *Bull. Chem. Soc. Jpn.* **44**, 3216-3216, doi:10.1246/bcsj.44.3216 (1971).

43 Kitano, M. *et al.* Ammonia synthesis using a stable electride as an electron donor and reversible hydrogen store. *Nat. Chem.* **4**, 934-940, doi:10.1038/nchem.1476 (2012).

44 Ogura, Y. *et al.* Effect of Calcination and Reduction Temperatures on the Catalytic Activity of Ru/$La_{0.5}Ce_{0.5}O_{1.75}$ for Ammonia Synthesis under Mild Conditions. *Energy Technol.* **8**, doi:10.1002/ente.202000264 (2020).

45 Siporin, S. Use of kinetic models to explore the role of base promoters on Ru/MgO ammonia synthesis catalysts. *J. Catal.* **225**, 359-368, doi:10.1016/j.jcat.2004.03.046 (2004).

46 Kinoshita, N., Kido, K., Domen, K., Aika, K. & Onishi, T. Behaviour of dinitrogen species adsorbed on a Co/Al_2O_3 catalyst

with or without coadsorbed hydrogen studied by infrared spectroscopy. *J. Chem. Soc, Faraday Trans. 1: Physical Chemistry in Condensed Phases* **82**, doi:10.1039/f19868202269 (1986).

47 Kubota, J. & Aika, K. Infrared spectra of adsorbed dinitrogen on ruthenium metal supported on alumina and magnesium oxide. *J. Chem. Soc., Chem. Commun.*, 1544, doi:10.1039/c39910001544 (1991).

48 Kubota, J. & Aika, K. Infrared Studies of Adsorbed Dinitrogen on Supported Ruthenium Catalysts for Ammonia Synthesis: Effects of the Alumina and Magnesia Supports and the Cesium Compound Promoter. *J. Phys. Chem.* **98**, 11293-11300, doi:10.1021/j100095a010 (1994).

49 Wiberg, K. B. Application of the pople-santry-segal CNDO method to the cyclopropylcarbinyl and cyclobutyl cation and to bicyclobutane. *Tetrahedron* **24**, 1083-1096, doi:10.1016/0040-4020(68)88057-3 (1968).

50 Lutz, H. D., Eckers, W., Schneider, G. & Haeuseler, H. Raman and infrared spectra of barium and strontium hydroxides and hydroxide hydrates. *Spectrochim. Acta, Part A* **37**, 561-567, doi:10.1016/0584-8539(81)80048-7 (1981).

51 Roedel, E., Urakawa, A., Kureti, S. & Baiker, A. On the local sensitivity of different IR techniques: Ba species relevant in NO_x storage-reduction. *Phys. Chem. Chem. Phys.* **10**, 6190-6198, doi:10.1039/b808529c (2008).